Spin to charge current conversion by the inverse spin Hall effect in the metallic antiferromagnet Mn_2Au at room temperature

M. Arana,[1,2,*] M. Gamino,[1] E. F. Silva,[1] V. M. T. S. Barthem,[2,3] D. Givord,[2,3] A. Azevedo,[1] and S. M. Rezende[1]

[1]*Departamento de Física, Universidade Federal de Pernambuco, 50670-901 Recife, PE, Brazil*

[2]*Instituto de Física, Universidade Federal do Rio de Janeiro, 21941-909 Rio de Janeiro, RJ, Brazil*

[3]*Centre National de la Recherche Scientifique–Université Grenoble Alpes, Institut Néel, F-38000 Grenoble, France*

(Received 14 July 2018; published 23 October 2018)

We report experiments demonstrating the spin to charge current conversion by means of the inverse spin Hall effect in ultrathin films of the metallic antiferromagnet Mn_2Au at room temperature. The Mn_2Au films, of different thicknesses, were grown by dc sputtering directly onto crystalline films of the ferrimagnetic insulator yttrium iron garnet (YIG). The spin currents are generated in the YIG film by two different processes, spin pumping effect (SPE) and spin Seebeck effect (SSE). In the SPE experiments we use microwave-driven ferromagnetic resonance of the YIG film to generate a spin current that is injected into the Mn_2Au, while in the SSE experiments the spin current is generated by a thermal gradient across the YIG film in the configuration of the longitudinal spin Seebeck effect. From these measurements, we obtain for Mn_2Au at room temperature a spin-diffusion length, λ_S, of 1.6 nm and a spin Hall angle, $\theta_{SH} \approx 0.04$, which is comparable to the value for platinum.

DOI: 10.1103/PhysRevB.98.144431

I. INTRODUCTION

The conversion of charge currents into spin currents and vice versa are key phenomena for spintronics because they make it possible to encode and decode information carried by electric signals into and out of the spin channel. These phenomena require materials with significant spin-orbit coupling and are made possible by two mechanisms, namely, the spin Hall effect [1–5] and the Rashba-Edelstein effect [6–10]. A major difference between these two processes is that the spin Hall effect is basically a bulk effect, whereas the Rashba-Edelstein effect is observed at interfaces [6–12] or in systems where the spins and electrons are confined to a two-dimensional state, such as graphene [13] and topological insulators [14–19]. The spin Hall effect (SHE) and its Onsager reciprocal, the inverse spin Hall effect (ISHE), have been extensively studied in films of paramagnetic metals with heavy elements [1–5,20–25], such as Pt, Pd, W, and Ta, and in paramagnetic semiconductors, such as Si, Ge, GaAs, and (GaMn)As [26–32].

The feasibility of using magnetic metals as ISHE spin detectors was first demonstrated in films of ferromagnetic (FM) permalloy ($Fe_{19}Ni_{81}$) [20]. However, in FM metals the anisotropic magnetoresistance and other spurious effects complicate the interpretation of the experiments [23,24] and also limit possible applications with dynamic phenomena [33]. Traditionally antiferromagnetic (AF) materials had only one practical application, namely, pinning an adjacent FM magnetization in spin-valve devices [34] through the interfacial exchange bias [35,36]. The possibility of using metallic antiferromagnetic materials in spintronics for other functionalities was first motivated by theoretical calculations showing the large anomalous Hall conductivity of γ-$IrMn_3$, a high-temperature noncollinear AF with zero net magnetization [37]. This prediction was greeted with large expectations. A large ISHE predicted for IrMn was first demonstrated in spin to charge current conversion experiments using spin pumping effect (SPE) and spin Seebeck effect (SSE) techniques [38]. Subsequently ISHE was also observed with SPE experiments in bilayers of $X_{50}Mn_{50}$ films, with X = Fe, Pd, Ir, Pt [39,40], confirming the potential use of metallic AFs as spin detector materials. These discoveries contributed to attract additional attention to AF materials in spintronics [41–47].

In this paper we report the observation of ISHE in Mn_2Au, a recently discovered metallic AF with very high Néel temperature $T_N \approx 1350$ K and unique AF properties, first predicted theoretically [48,49] and subsequently confirmed by experiments [50]. After that, Mn_2Au has attracted increasing attention [51–56] and the determination of new properties directly related to spin dynamics became an urgent challenge towards new applications of this material in spintronics. Here we show that it also has a large spin Hall angle and can be used as a good spin current detector. The spin currents are generated by two different schemes, microwave driven spin pumping and the spin Seebeck effect. In Sec. II we describe the samples preparation, structure characterization by x-ray diffraction, and magnetic characterization by ferromagnetic resonance. In Sec. III we present theoretical considerations and the experimental results with ferromagnetic resonance (FMR) driven by SPE. In Sec. IV we present theoretical considerations and measurements with the SSE and in Sec. V we compare the results of the two techniques and show how to obtain the spin-diffusion length and the spin Hall angle.

*Corresponding author: arana@df.ufpe.br

II. SAMPLE PREPARATION AND CHARACTERIZATION

The experiments reported here were carried out with bilayers made of the ferrimagnetic insulator (FMI) yttrium iron garnet (YIG-$Y_3Fe_5O_{12}$) and the metallic antiferromagnets Mn_2Au. YIG (111) single-crystal films were grown by liquid phase epitaxy onto [111]-oriented $Gd_3Ga_5O_{12}$ (GGG) substrates with thickness 0.5 mm. The growth was made at constant temperature, between 1000 and 1050 °C, in supersaturated solutions using PbO-B_2O_3 based flux by the horizontal dipping technique. The substrate was immersed in the melt for typically 3 min and rotated continuously at a rate of 100 rpm while film growth took place, with growth rate between 1 and 3 μm/min. The YIG film thus obtained on top of the GGG substrate was 6 μm thick. The substrate was subsequently cut in the form of rectangles with lateral dimensions $2.0 \times 3.5\,\mathrm{mm}^2$.

Since the spin to charge conversion requires thin films with thicknesses comparable to the spin-diffusion length,[1] for this paper we have produced Mn_2Au films with thicknesses of a few nanometers (3 to 10 nm thick). The bimetallic compound Mn_2Au was prepared from an initial Au/Mn/Au trilayer and a posterior thermal treatment leading to atomic interdiffusion of Au and Mn. The two Au individual layers and the Mn layer were sequentially deposited by dc sputtering directly on top of the small GGG/YIG rectangular substrates at room temperature. The film total thickness is, in principle, related to the individual layer thicknesses by

$$t_{Mn_2Au} = t_{Au}\frac{\rho_{Au}}{\rho_{Mn_2Au}} + t_{Mn}\frac{\rho_{Mn}}{\rho_{Mn_2Au}}$$

with $t_{Mn} = 2t_{Au}\frac{\rho_{Au}}{\rho_{Mn}}\frac{M_{Mn}}{M_{Au}}$ to respect the expected Mn_2Au stoichiometry. However, it was found that a 70% excess of Mn, compared to the stoichiometric formula, was necessary to obtain the Mn_2Au phase. This was attributed to the fact that Mn atoms are easily lost during thermal treatment. The subsequent thermal treatment consisted in heating the samples in the sputtering chamber under a pressure of 10^{-7} torr, at a rate of 10 °C/min, up to 400 °C, and keeping the sample at this temperature for 3 h. The upper Au layer reduces Mn evaporation during the thermal treatment and the lower Au layer avoids Mn diffusion in the YIG layer.

A test 10-nm-thick Mn_2Au sample was prepared and observed by TEM (Jeol JEM 2100F). Images obtained at 50 different positions were analyzed using the ImageJ software. The derived thickness amounted to 9.5(±0.7) nm in good agreement with expectation. The thicknesses of all other samples were assumed equal to expectation as described above.

The structure characterization was performed with a Rigaku x-ray diffractometer, model Smartlab, with the Cu K-α radiation ($\lambda = 1.5418$ Å), using theta-2 theta x-ray diffraction (XRD) and grazing incidence diffractometry (GIXRD) techniques. Figure 1(a) shows the theta-2theta XRD

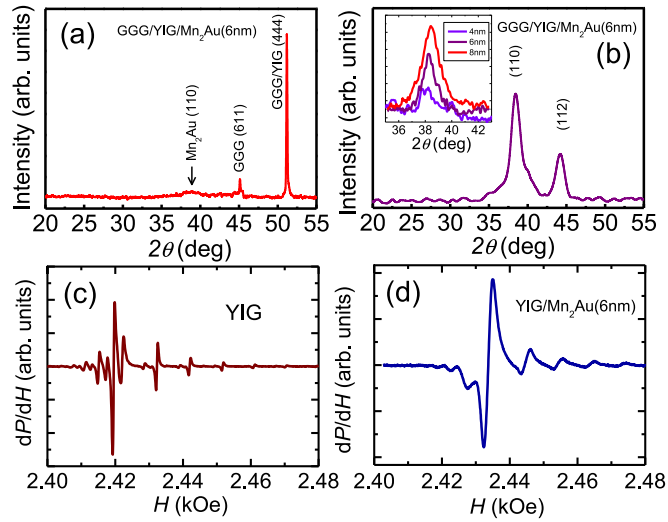

FIG. 1. Conventional x-ray-diffraction (a) and grazing incidence XRD (b) patterns of sample GGG/YIG (6 μm)/Mn_2Au (6 nm). (c), (d) Field scan microwave absorption derivative spectra at a frequency 9.4 GHz of 6-μm-thick YIG film with lateral dimensions $2.0 \times 3.5\,\mathrm{mm}^2$ with the magnetic field applied in the film plane, normal to the long dimension. In (c) the YIG film is bare, while in (d) it is covered with a Mn_2Au (6 nm) layer. The inset of (b) shows the [110] peak for samples with thickness 4, 6, and 8 nm.

pattern of GGG/YIG (6 μm), exhibiting the double peak at $2\theta = 51.23$ and 51.10°, respectively, corresponding to the (444) Bragg reflections of the GGG substrate and the (444) reflection of the YIG film, epitaxially grown on GGG. On the same patterns, the weak peak at $2\theta = 38.40°$ is the only one characteristic of the Mn_2Au, thus indicating 110 texture. GIXRD was used to minimize the contributions of the substrate and of the YIG film and reveal diffraction peaks characteristic of the Mn_2Au films. Figure 1(b) shows GIXRD for a Mn_2Au 6-nm-thick film, evidencing that the film is polycrystalline, with the [110] direction preferentially perpendicular to the substrate surface, so that reflections at $2\theta = 38.40$ and 44.10° corresponding to the (110) and (112) planes, respectively, are present. The (110) reflection peak obtained from GIXRD measurements of samples GGG/YIG (6 μm)/Mn_2Au (t nm) for $t = 4$, 6, and 8 nm is shown for comparison as an inset of Fig. 2(b). From the inset, it is clear that the samples' crystallinity is good in every case, increasing with the thickness increment.

For the microwave FMR and spin pumping experiments, the sample with the structure shown in Fig. 2(a) was mounted on the tip of a polyvinyl chloride (PVC) rod and inserted into a small hole in the back wall of a shorted X-band waveguide, in a position of maximum rf magnetic field and zero electric field. We did not use a microwave cavity because the detuning of its resonance at the strong FMR absorption of YIG introduces distortions in the line shapes. The waveguide is placed between the poles of an electromagnet so that the sample can be rotated while maintaining the quasistatic and rf fields in the film plane and perpendicular to each other. With this configuration we can investigate the angular dependence of the spectra. Figure 1(c) shows the field scan FMR microwave absorption derivative dP/dH of the bare YIG film

[1]In principle, the charge current does not disappear but saturates at large thicknesses. However, the signal measured is a voltage, inversely proportional to the sample resistance [see Eqs. (6), (7), (10), and (11)], and thus the signal is maximum at film thickness of the order of λ.

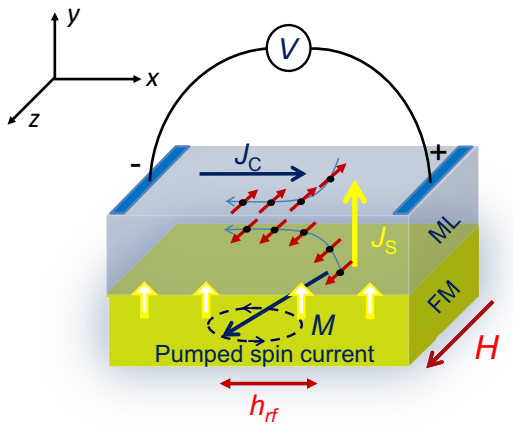

FIG. 2. Illustration of the ferromagnetic (Fm)/metallic layer (ML) structure used for the studies of the FMR spin pumping effect and coordinate system. The microwave magnetic field that drives the FMR is perpendicular to the static magnetic field H that defines the direction of the spin polarization of the spin current. The electrodes at the edges are used to measure the dc voltage due to the charge current resulting from the conversion of the spin current by the inverse spin Hall effect.

(6 μm × 2.0 mm × 3.5 mm) with the quasistatic field along z (see Fig. 2) and modulated at 1.2 kHz with a pair of Helmholtz coils. The measurements were done with input microwave power up to 63 mW, small enough to avoid nonlinear effects [57] with the shorted waveguide setup. The spectrum in Fig. 1(c) obtained before deposition of the Mn_2Au layer on the YIG film allows a clear identification of the absorption lines. They correspond [58] to standing spin-wave modes that have quantized in-plane wave numbers $k_x = n_x\pi/L_x$ and $k_z = n_z\pi/L_z$ due to the boundary conditions at the edges of the film with lateral dimensions L_x and L_z. The strongest line corresponds to the FMR mode with $n_x = 1$, $n_z = 1$, that has frequency close to the one for the spin wave with $k = 0$ given by the Kittel equation [59]

$$\omega_0 = \gamma(H + H_A)^{1/2}(H + H_A + 4\pi M + H_S)^{1/2}, \quad (1)$$

where γ is the gyromagnetic ratio ($\gamma = g\mu_B/\hbar = 2\pi \times 2.8\,\mathrm{GHz/kOe}$ for YIG), $4\pi M$ is the spontaneous magnetization (1.76 kG at room temperature), and H_A and H_S are, respectively, the in-plane and the out-of-plane (surface) anisotropy fields. The lines to the left of the FMR correspond to hybridized standing spin-wave surface modes whereas those to the right are volume modes. All modes have similar peak-to-peak linewidth of 1.4 Oe, corresponding to a half width at half maximum of $\Delta H \approx 1.2$ Oe.

As can be seen in Fig. 1(d), in YIG/Mn_2Au bilayers, the FMR linewidth is increased to $\Delta H_{\mathrm{YIG/Mn_2Au}} = 2.0$ Oe, due to the fact that the spin current created by spin pumping carries angular momentum out of the YIG film [60,61]. As will be discussed later, from the line broadening, we can obtain a good estimate for the spin mixing conductance, necessary to calculate the spin Hall angle from the SPE and SSE experiments.

III. SPIN PUMPING EFFECT

A. Theoretical considerations

Figure 2 illustrates the sample arrangement used to study the spin pumping effect, where the magnetization in the ferro- or ferromagnetic film is driven by a rf magnetic field $\hat{x}h_{rf}\exp(i\omega t)$ with microwave frequency $\omega = 2\pi f$ perpendicular to the static field $\hat{z}H$, in the configuration of the FMR experiments. The voltage generated in the adjacent metallic layer (ML) has its origin in two combined processes, the spin pumping mechanism devised by Silsbee *et al.* [62] and Tserkovnyak *et al.* [60,61] and the ISHE identified by Saitoh *et al.* [22]. In Refs. [60,61] it is shown that a precessing magnetization in the FM layer injects a pure spin current into the adjacent ML with density given by $\vec{J_S} = (\frac{\hbar g_{\mathrm{eff}}^{\uparrow\downarrow}}{4\pi M^2})(\vec{M} \times \partial\vec{M}/\partial t)$, where $g_{\mathrm{eff}}^{\uparrow\downarrow}$ is the real part of the effective spin mixing conductance at the interface that takes into account the spin pumped and back-flow spin currents. Writing the time dependence of the magnetization as $\vec{M}(t) = \hat{z}M_z + (\hat{x}m_x + \hat{y}m_y)\exp(i\omega t)$, where $m_x,\ m_y \ll M_z$, the dc spin current with polarization along z at the FM/ML interface ($y = 0$) becomes

$$J_S(0) = \frac{\hbar\omega g_{\mathrm{eff}}^{\uparrow\downarrow}}{4\pi M^2}\mathrm{Im}(m_x^* m_y). \quad (2)$$

Using the Landau-Lifshitz equation with the dipolar field appropriate for a film magnetized in the plane, and introducing the relaxation in a phenomenological manner, we can obtain the relations between the rf magnetization components in the x and y directions and the driving rf magnetic field:

$$m_x = \frac{\gamma(H + 4\pi M_{\mathrm{eff}})\gamma M_{\mathrm{eff}}}{(\omega_0^2 - \omega^2) + i2\omega_0\eta}h_{\mathrm{rf}}, \quad (3)$$

$$m_y = -i\frac{\omega\gamma M_{\mathrm{eff}}}{(\omega_0^2 - \omega^2) + i2\omega_0\eta}h_{\mathrm{rf}}, \quad (4)$$

where ω_0 is the FMR frequency for the film, given by Eq. (1), $4\pi M_{\mathrm{eff}} = 4\pi M + H_S$ is the effective magnetization, and η is the magnetic relaxation rate, related to the Gilbert damping parameter α by $\eta = \omega\alpha$. Since the measurements are done at a fixed frequency ω and varying field H we must express ω_0 and η in terms of H, ω and of the field for resonance H_r (the field at which the resonance is at the frequency ω). Using Eq. (1) we express the relaxation rate in terms of the half linewidth at half maximum ΔH, $\eta = \gamma\Delta H(2H_r + 4\pi M_{\mathrm{eff}})/2(H_r^2 + H_r 4\pi M_{\mathrm{eff}})^{1/2}$, and substitute Eqs. (3) and (4) in Eq. (2) to obtain the spin current density pumped through the FMI/ML interface:

$$J_S(0) = \frac{\hbar\omega g_{\mathrm{eff}}^{\uparrow\downarrow} p}{16\pi}\left(\frac{h_{\mathrm{rf}}}{\Delta H}\right)^2 L(H - H_r), \quad (5)$$

where $L(H - H_r) = \Delta H^2/[(H - H_r)^2 + \Delta H^2]$ is the Lorentzian function and p is the ellipticity factor $p = 4\omega(H_r + 4\pi M_{\mathrm{eff}})/\gamma(2H_r + 4\pi M_{\mathrm{eff}})^2$. The spin current that flows through the FMI/ML interface produces a pure spin current in the ML, formed by charge carriers with opposite spins moving in opposite directions and given by the gradient of the spin accumulation [59,60]. This spin current diffuses into the ML with a current density that can be expressed as

$J_S(y) = J_S(0)\{\sinh[(t-y)/\lambda_S]/\sinh(t/\lambda_S)\}$, where t and λ_S are, respectively, the thickness and spin-flip diffusion length of the metallic layer. Then, due to the ISHE, a fraction of the charge carriers undergoes spin-orbit scattering generating a transverse charge motion with current density $\overrightarrow{J_C}$ given by $\overrightarrow{J_C} = \theta_{\rm SH}(2e/\hbar)\overrightarrow{J_S} \times \hat{\sigma}$, where $\theta_{\rm SH}$ is the spin Hall angle and $\hat{\sigma}$ is the spin polarization. This produces a dc voltage along the length L of the metallic layer that is measured between the contacts placed at the two ends of the sample, as illustrated in Fig. 2. Integration of the charge current density along x and y gives for the spin pumping voltage [24]:

$$V_{\rm SPE} = Rw\lambda_S \frac{2e}{\hbar}\theta_{\rm SH} \tanh\left(\frac{t}{2\lambda_S}\right) J_S(0), \tag{6}$$

where R and w are, respectively, the resistance and width of the ML strip. Finally, replacing in Eq. (6) $J_s(0)$ as given by Eq. (5), we obtain for the peak amplitude of the spin pumping ISHE voltage at the field for resonance $H = H_r$, with $L(H = H_r) = 1$,

$$V_{\rm SPE}^{\rm peak} = \left(\frac{1}{4}\right) Rw\lambda_S e\theta_{\rm SH} f g_{\rm eff}^{\uparrow\downarrow} p_{xz} \tanh\left(\frac{t}{2\lambda_S}\right)\left(\frac{h_{\rm rf}}{\Delta H}\right)^2, \tag{7}$$

where p_{xz} is a factor that expresses the ellipticity and the spatial variation of the rf magnetization of the FMR mode. This result will be used in the next section to obtain the spin Hall angle from the spin pumping measurements.

B. Experimental results

We have chosen to use a film of insulating ferrimagnetic YIG as the source of the FMR spin pumping current so that the voltage measured in the Mn_2Au layer is free from the contamination of spin rectification and magnonic charge pumping effects, present in metallic ferromagnets, such as permalloy [23,24,63]. The spin pumping ISHE experiments were carried out with a YIG/Mn_2Au sample arrangement as illustrated in Fig. 2. In order to compare the data with the ones in a well-characterized nonmagnetic metal, we have also made a similar bilayer structure with a 4-nm-thick Pt film sputter deposited on a YIG film. As mentioned earlier, the sample is mounted on the tip of a PVC rod and inserted into a small hole in the back wall of a shorted x-band waveguide, in a position of maximum rf magnetic field and zero electric field, with the static magnetic field in the film plane. All experiments described here were carried out using a microwave frequency of 9.4 GHz and at room temperature.

Figure 3(a) shows the spin pumping ISHE voltage measured in YIG/Mn_2Au (4 nm) with a magnetic field applied in the film plane perpendicularly to the long strip dimension, and scanned around the values leading to resonance, for several values of the input microwave power P_i. The voltage spectra show a large peak corresponding to the FMR mode and several lateral peaks corresponding to the resonances of the magnetostatic modes [64,65]. We note that in the SPE the spin current generated by the precessing magnetization in the YIG film flows in the $+y$ direction. Since the polarization is in the $+z$ direction, a charge current by $\overrightarrow{J_C} = \theta_{\rm SH}\overrightarrow{J_S} \times \hat{\sigma}$ flowing in the $+x$ direction implies a positive spin Hall angle by $\theta_{\rm SH}$.

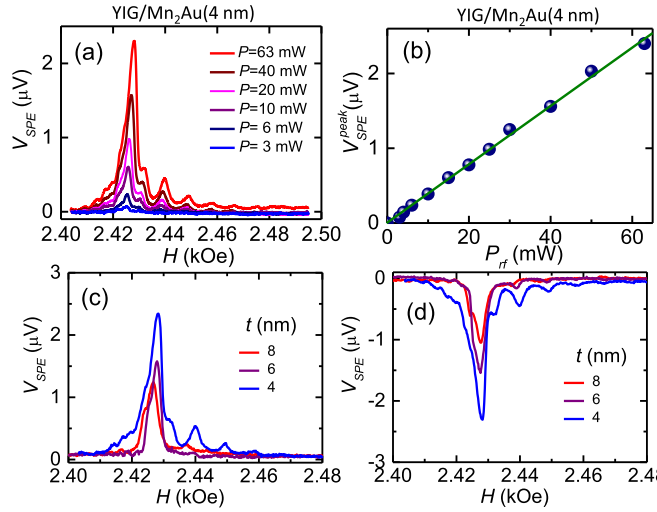

FIG. 3. (a) Field scan spin pumping ISHE voltage produced by FMR microwave excitation at a frequency 9.4 GHz in a bilayer of YIG (6 μm)/Mn_2Au (4 nm) for several values of the rf microwave power as indicated. (b) Plot of the voltage peak amplitude as a function of the microwave power. (c) Voltage vs field measured in three YIG/Mn_2Au (t) samples with thickness $t = 4$, 6, and 8 nm, for the applied field in the direction indicated in Fig. 2, and for a microwave power $P_{\rm rf} = 63$ mW. (d) Same as in (c) with the field in the opposite direction.

Hence, the positive signs of the voltages in Fig. 3(a) show that Mn_2Au has by $\theta_{\rm SH} > 0$ the same sign as in Pt. Figure 3(b) shows that the voltage peak amplitude for the FMR mode measured as in Fig. 3(a) varies linearly with microwave input power P_i, consistent with Eq. (7) for the spin pumping process. Figure 3(c) shows the voltage versus field measured in three YIG/Mn_2Au (t) samples with thickness $t = 4$, 6, and 8 nm, for the field applied along z, with the same direction as in Fig. 2, while Fig. 3(d) shows the voltage with the field in the opposite direction. The change in the voltage sign with the reversal of the field is due to the reversal of the spin polarization by $\hat{\sigma}$, and represents another confirmation of the spin pumping ISHE nature of the voltage. If the sample is rotated by 90° so that the field is in the direction of the current, the signal falls to the noise level, as expected.

In order to obtain the spin Hall angle of Mn_2Au from the measured voltage using Eq. (7), we need to know the effective spin mixing conductance $g_{\rm eff}^{\uparrow\downarrow}$ for the YIG/Mn_2Au interface. This can be inferred from the broadening of the FMR linewidth due to the spin pumping process using $g_{\rm eff}^{\uparrow\downarrow} = (4\pi M_S t_{\rm coh}/\hbar\omega)\delta H$, where δH is the additional FMR linewidth due to the spin pumping process and $t_{\rm coh}$ is a coherence length for thick YIG films [66]. Since $t_{\rm coh}$ depends on various conditions, we determined the spin mixing conductance by comparing the FMR line broadening in YIG/Mn_2Au with that in YIG/Pt. The deposition of the Mn_2Au layer on the YIG film leads to an increase in the FMR linewidth of 0.8 Oe at 9.4 GHz, while deposition of Pt increases the linewidth by 0.56 Oe. Considering that the interface of YIG/Pt has an effective spin mixing conductance of $g_{\rm eff}^{\uparrow\downarrow} = 10^{14}$ cm^{-2} [67–70], we derive for the YIG/Mn_2Au interface a value $g_{\rm eff}^{\uparrow\downarrow} = 1.4 \times 10^{14}$ cm^{-2}.

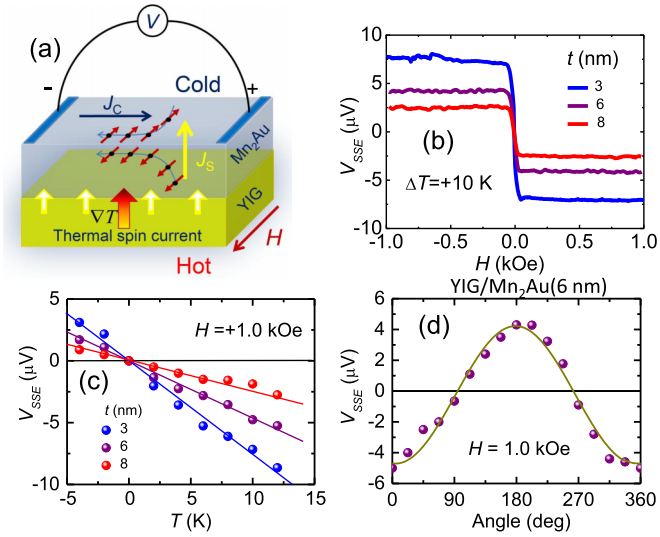

FIG. 4. (a) Schematic illustration of the sample structure used to measure the voltages generated in YIG/Mn_2Au by the spin Seebeck effect. (b) Variation with magnetic field of the SSE voltage measured in the $Mn_2Au(t)$ layer with $t = 3$, 6, and 8 nm, with the temperature difference $\Delta T = +10$ K. Positive ΔT indicates that the Mn_2Au layer is warmer than the substrate. (c) SSE voltage vs temperature difference measured with $H = +1.0$ kOe. (d) Variation of the SSE voltage with the magnetic field angle measured with $H = +1.0$ kOe and $\Delta T = +10$ K in sample GGG/YIG (6 um)/Mn_2Au (6 nm). The solid curve is a fit with $A\cos\phi$.

The driving rf field at the back wall of the rectangular X-band waveguide that enters in Eq. (7) is obtained from the electromagnetic field in the TE_{10} mode [71], $h_{\rm rf} = 2P_{\rm rf}^{1/2}/(f\mu_0\lambda_g ab)^{1/2}$, where P is the microwave power, λ_g; a and b are, respectively, the guide wavelength and the two inner waveguide dimensions; and μ_0 is the vacuum permeability. Using the dimensions $a = 2.3$ cm and $b = 1.1$ cm for the x-band waveguide, we obtain for 9.4 GHz a rf field in Oersted, $h_{\rm rf} = 0.138P^{1/2}$, with P in watts. For a microwave power of 63 mW, used in the measurements of Fig. 2(c), we have $h_{\rm rf} = 3.5 \times 10^{-2}$ Oe. Consider for Mn_2Au a spin-diffusion length, $\lambda_S = 1.6$ nm (see Sec. V), which is similar to values in other metallic AFs with Mn [39]; for a sufficiently thick sample, this gives $\tanh(t/2\lambda_S) \approx 1$. Using $w = 0.2$ cm, $p_{1,1} = 0.31$ appropriate for the uniform (1,1) mode in YIG at 9.4 GHz [38], and the values measured for the present samples, $t = 6.0$ nm, $R = 240\,\Omega$, $\Delta H = 2.0$ Oe, and $V_{\rm SPE}^{\rm peak} = 1.4\,\mu$V, a spin Hall angle $\theta_{\rm SH} = 0.037$ is derived from Eq. (7). This value can be compared to that of platinum, about 0.1, one of the materials with highest spin Hall effect [72].

IV. SPIN SEEBECK EFFECT EXPERIMENTS

In order to confirm the spin to charge current conversion in Mn_2Au by the ISHE, we have used another process to generate the spin current, namely, the SSE in the longitudinal configuration [73–81]. Figure 4(a) illustrates the sample arrangement for the SSE experiments, where the temperature difference across the bilayer is produced by a Peltier module. As shown in Refs. [76,79,82], the temperature gradient across the thickness of the insulating FM layer produces a drift-diffusion motion of thermal magnons, producing a spin current in the FM layer that flows across the FM/ML interface. Using the Boltzmann equation and the diffusion equation to describe the magnonic spin transport, subject to the appropriate boundary conditions, the spin current density at the interface created by a temperature gradient in the y direction is given by [76,80,82]

$$J_S(0) = -C_s\rho g_{\rm eff}^{\uparrow\downarrow}\nabla_y T, \tag{8}$$

where C_s is a coefficient that depends on the material parameters, temperature, and applied field intensity [see Eq. (45) in Ref. [82]], and ρ is a factor that represents the effect of the finite thickness of the FM layer, given by

$$\rho = \frac{\cosh\left(\frac{t_{\rm FM}}{l_m}\right) - 1}{\sinh\left(\frac{t_{\rm FM}}{l_m}\right)}, \tag{9}$$

where $t_{\rm FM}$ and l_m are, respectively, the thickness and the magnon diffusion length of the FM layer. The thickness factor is such that $\rho \approx 1$ for $t_{\rm FM} \gg l_{\rm m}$ and $\rho \approx 0$ for $t_{\rm FM} \ll l_{\rm m}$. Note that while in SPE the spin current always flows from the FM into the ML ($+y$ direction), in SSE the direction depends on the signs of the gradient and of the coefficient C_s. For YIG/Pt, $C_s > 0$, so that for $\nabla T > 0$ (FM cooler than ML) the current flows from the ML into the FM layer, which is the direction opposite to the SPE. On the other hand, for $\nabla T > 0$ (ML cooler than FM), the current flows from the FM into the ML.

The spin current $\vec{J_S}$ flowing into the metallic layer diffuses with diffusion length λ_S, and generates a charge current density $\vec{J_C} = \theta_{\rm SH}(2e/\hbar)\vec{J_S} \times \hat{\sigma}$, that produces a SSE voltage in the ML layer. Similarly, to the SPE, the voltage is obtained by integrating the charge current density along x and y and is given by

$$V = F_P R w \lambda_S \frac{2e}{\hbar}\theta_{\rm SH}\tanh\left(\frac{t}{2\lambda_S}\right) J_S(0)\cos\phi, \tag{10}$$

where λ_S, R, t, and w, respectively, are the spin-diffusion length, resistance, and thickness and width of the ML strip, and ϕ is the angle of the applied magnetic field H with the direction z transverse to the long dimension of the strip. The factor F_P introduced in Eq. (10) represents the fraction of the bilayer strip length covered by the Peltier module, where the spin current is generated. Replacing $J_s(0)$ in Eq. (10) by its expression in Eq. (8), we obtain the voltage due to the SSE-ISHE effects:

$$V_{\rm SEE} = -F_P R w \lambda_S \frac{2e}{\hbar}\theta_{\rm SH}\tanh\left(\frac{t}{2\lambda_S}\right) C_s\rho g_{\rm eff}^{\uparrow\downarrow}\nabla_y T\cos\phi. \tag{11}$$

The SSE experiments were carried out with the sample arrangement illustrated in Fig. 4(a). A commercial Peltier module of width 2 mm is used to heat or cool the side of the metallic layer, while the other side of the sample is in thermal contact with a copper block maintained at room temperature. The temperature difference ΔT across the GGG/YIG/Mn_2Au sample is measured using a differential thermocouple, with one junction attached to a thin copper strip placed between the

Peltier module and the sample structure and the other attached to the copper block. After calibration, the thin copper strip and the thermocouple were removed so as not to interfere in the SSE measurements. Figure 4(b) shows the variation of the measured voltage in the three samples with the magnetic field, H, applied along z, as in Fig. 4(a), for a temperature difference $\Delta T = +10\,\mathrm{K}$ (positive ΔT means that the ML is warmer than the copper base). The change in the sign of the voltage with the reversal in the direction of the field is due to the change in the sign of the spin polarization. Figure 4(c) shows the measured variation of the voltage, in the three samples, with the temperature difference ΔT, for a field $H = 1\,\mathrm{kOe}$. As stated above, since YIG is an insulator, the voltage measured in the Mn_2Au is entirely due to the spin Seebeck effect. Both data exhibit the features expected for the SSE, i.e., the SSE changes sign with the reversal of the field due to the reversal of the spin polarization and it varies linearly with ΔT as predicted by Eq. (11). In addition, the SSE varies according to $\cos\phi$, where ϕ is the angle between z and H [see Eq. (11)]. This is shown in Fig. 4(d) for a sample width $t = 6\,\mathrm{nm}$, $H = 1\,\mathrm{kOe}$, and temperature difference $\Delta T = +10\,\mathrm{K}$. Similar results were obtained with the other samples.

From the SSE data in Fig. 4 we can also obtain an estimative for the spin Hall angle of Mn_2Au. For this we use the value of the SSE parameter in Ref. [80], $C_s = 3.3 \times 10^{-24}\,\mathrm{erg\,cm^{-1}\,K^{-1}}$, and the same parameters for Mn_2Au (6 nm) used in Sec. III, namely, $w = 0.2\,\mathrm{cm}$, $R = 240\,\Omega$, $g_{\mathrm{eff}}^{\uparrow\downarrow} = 1.4 \times 10^{14}\,\mathrm{cm^{-2}}$, $\lambda_S = 1.6\,\mathrm{nm}$ (see Sec. V below), and $F_P = 2.0/3.0$. With the measured value of μV under $H = +1\,\mathrm{kOe}$, with $\Delta T = +10\,\mathrm{K}$, corresponding to a temperature gradient $\nabla_y T = +200\,\mathrm{K/cm}$, we obtain from Eq. (11) a spin Hall angle $\theta_{\mathrm{SH}} \approx 0.031$, similar to the one measured with the spin pumping experiments.

V. DISCUSSION AND CONCLUSIONS

As shown in the previous sections, we have used the spin pumping effect and the spin Seebeck effect in YIG to inject spin currents in several films of Mn_2Au. We will show in this discussion that the results obtained with the two techniques are fully consistent. It is possible to determine both parameters θ_{SH} and λ_S, by fitting the theoretical expressions to the measured voltages in several samples with thickness comparable to λ_S [39]. We have done this with the data obtained both with the SPE and SSE experiments. Considering the peak of the SPE current at $H = H_r$, related to the peak of the SPE voltage by $I_{\mathrm{SPE}}^{\mathrm{peak}} = I_{\mathrm{SPE}}^{\mathrm{peak}}/R$, with $L(H = H_r) = 1$, from Eq. (7) we have

$$\theta_{\mathrm{SH}} = \frac{4I_{\mathrm{SP}}^{\mathrm{peak}}}{w\lambda_S e f g_{\mathrm{eff}}^{\uparrow\downarrow} p_{xz} \tanh\left(\frac{t}{2\lambda_S}\right)(h_{\mathrm{rf}}/\Delta H)^2}. \quad (12)$$

Using the various parameters already given in Sec. III in Eq. (12), and assuming a microwave power of 63 mW, we obtain a relation between the spin Hall angle, the spin-diffusion length, and the measured SPE current:

$$\Theta_{\mathrm{SPE}} = \theta_{\mathrm{SH}}\lambda_S(\mathrm{nm}) \times \tanh\left(\frac{t}{2\lambda_S}\right) = 1.0 \times 10^{-3} \times I_{\mathrm{SPE}}^{\mathrm{peak}}(\mathrm{nA}). \quad (13)$$

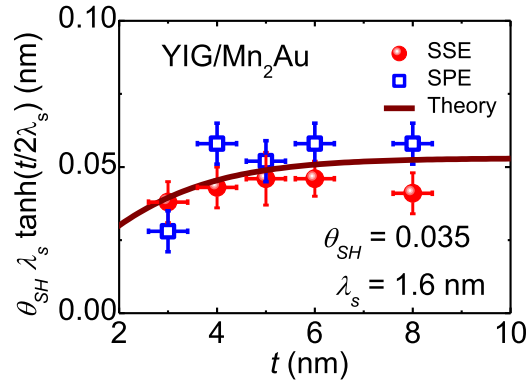

FIG. 5. Symbols: Data points calculated, for the charge current due to the spin pumping effect (SPE) and to the spin Seebeck effect (SSE), respectively. The current is multiplied by the factors given in Eqs. (13) and (14). Solid line: Best fit to the data, using the function in the vertical axis [see Eqs. (13) and (14)].

Similarly, with the parameters given in Sec. IV, we obtain another relation, using the charge current measured in the SSE experiments, $I_{\mathrm{SSE}} = V_{\mathrm{SSE}}/(F_p R)$, for a temperature difference $\Delta T = +10\,\mathrm{K}$ and $H = +1\,\mathrm{kOe}$:

$$\Theta_{\mathrm{SSE}} = \theta_{\mathrm{SH}}\lambda_S(\mathrm{nm}) \times \tanh\left(\frac{t}{2\lambda_S}\right) = -1.71 \times 10^{-3} \times I_{\mathrm{SPE}}^{\mathrm{peak}}(\mathrm{nA}). \quad (14)$$

The symbols in Fig. 5 represent the values of the quantities in Eqs. (13) and (14) obtained from the currents measured in the SPE and SSE experiments, for five YIG/Mn_2Au (t) samples with $t = 3$, 4, 5, 6, and 8 nm. The data obtained from the SPE and SSE experiments are consistent with each other. The best fit to these experimental results (see Fig. 5) is obtained for $\lambda_S = (1.60 \pm 0.02)\,\mathrm{nm}$ and $\theta_{\mathrm{SH}} = (0.035 \pm 0.005)$.

In conclusion, we have demonstrated the spin to charge current conversion by means of the inverse spin Hall effect in the metallic antiferromagnet Mn_2Au at room temperature. The spin currents were generated in a film of the insulating ferrimagnet YIG by two different processes, spin pumping and spin Seebeck effects. In the first we have used microwave-driven ferromagnetic resonance of the YIG film to generate a spin current, while in the second the spin current was produced by a thermal gradient applied across the YIG film. We have shown that in both cases the spin current injected across the interface of the YIG/Mn_2Au bilayer is converted into a charge current in the Mn_2Au layer. Measurements done with both techniques in films of Mn_2Au with varying thickness are consistent with each other and from them we obtain a spin-diffusion length $\lambda_S = 1.6\,\mathrm{nm}$ and a spin Hall angle $\theta_{\mathrm{SH}} = 0.035$ for Mn_2Au at room temperature.

Compared to other metallic room-temperature antiferromagnets, Mn_2Au combines a large spin Hall angle with a relatively small resistivity ($\approx$20 $\mu\Omega$ cm). These results confirm its potential for spintronics applications.

ACKNOWLEDGMENTS

This research was supported by Conselho Nacional de Desenvolvimento Científico e Tecnológico (CNPq), Coordenação de Aperfeiçoamento de Pessoal de Nível Superior, Financiadora de Estudos e Projetos, and Fundação de Amparo à Ciência e Tecnologia do Estado de Pernambuco. M.A. and E.F.S. are grateful to CNPq for the grant of a postdoctoral fellowship associated to this project. The authors also would like to thank the Laboratório Multiusuário de Nanociência e Nanotecnologia/Centro Brasileiro de Pesquisas Físicas (LABNANO/CBPF) for technical support during electron microscopy work.

[1] M. I. D'yakonov and V. I. Perel, Spin relaxation of conduction electrons in non centrosymmetric semiconductors, Sov. Phys. Solid State **13**, 3023 (1972).

[2] J. E. Hirsh, Spin Hall Effect, Phys. Rev. Lett. **83**, 1834 (1999).

[3] A. Hoffmann, Spin Hall effects in metals, IEEE Trans. Mag. **49**, 5172 (2013).

[4] S. Maekawa, H. A. Adachi, K. Uchida, J. Ieda, and E. Saitoh, Spin current: Experimental and theoretical aspects, J. Phys. Soc. Jpn. **82**, 102002 (2013).

[5] J. Sinova, S. O. Valenzuela, J. Wunderlich, C. H. Back, and T. Jungwirth, Spin Hall effects, Rev. Mod. Phys. **87**, 1213 (2015).

[6] V. M. Edelstein, Spin polarization of conduction electrons induced by electric current in two-dimensional asymmetric electron systems, Solid State Commun. **73**, 233 (1990).

[7] A. Manchon, H. C. Koo, J. Nitta, S. M. Frolov, and R. A. Duine, New perspectives for Rashba spin-orbit coupling, Nat. Mater. **14**, 871 (2015).

[8] A. Soumyanarayanan, N. Reyren, A. Fert, and C. Panagopoulos, Emergent phenomena induced by spin-orbit coupling at surfaces and interfaces, Nature (London) **539**, 509 (2016).

[9] Y. Ando and M. Shiraishi, Spin to charge interconversion phenomena in the interface and surface states, J. Phys. Soc. Jpn. **86**, 011001 (2017).

[10] W. Han, Y. Otani, and S. Maekawa, Quantum materials for spin and charge conversion, NPJ Quantum Materials **3**, 27 (2018).

[11] J. C. Rojas Sánchez, L. Vila, G. Desfonds, S. Gambarelli, J. P. Attané, J. M. De Teresa, C. Magén, and A. Fert, Spin-to-charge conversion using Rashba coupling at the interface between non-magnetic materials, Nat. Commun. **4**, 2944 (2013).

[12] J. Sklenar, W. Zhang, M. B. Jungfleisch, W. Jiang, H. Saglam, J. E. Pearson, J. B. Ketterson, and A. Hoffmann, Perspective: Interface generation of spin-orbit torques, J. Appl. Phys. **120**, 180901 (2016).

[13] J. B. S. Mendes, O. Alves-Santos, L. M. Meireles, R. G. Lacerda, L. H. Vilela-Leão, F. L. A. Machado, R. L. Rodríguez-Suárez, A. Azevedo, and S. M. Rezende, Spin-Current to Charge-Current Conversion and Magnetoresistance in a Hybrid Structure of Graphene and Yttrium Iron Garnet, Phys. Rev. Lett. **115**, 226601 (2015).

[14] J.-C. Rojas-Sanchez, S. Oyarz´un, Y. Fu, A. Marty, C. Vergnaud, S. Gambarelli, L. Vila, M. Jamet, Y. Ohtsubo, A. Taleb-Ibrahimi, P. Le Fèvre, F. Bertran, N. Reyren, J.-M. George, and A. Fert, Spin to Charge Conversion at Room Temperature by Spin Pumping into a New Type of Topological Insulator: α-Sn Films, Phys. Rev. Lett. **116**, 096602 (2016).

[15] H. Wang, J. Kally, J. S. Lee, T. Liu, H. Chang, D. R. Hickey, K. A. Mkhoyan, M. Wu, A. Richardella, and N. H. Samarth, Surface-State-Dominated Spin-Charge Current Conversion in Topological-Insulator–Ferromagnetic-Insulator Heterostructures, Phys. Rev. Lett. **117**, 076601 (2016).

[16] K. Kondou, R. Yoshimi, A. Tsukazaki, Y. Fukuma, J. Matsuno, K. S. Takahashi, M. Kawasaki, Y. Tokura, and Y. Otani, Fermi-level-dependent charge-to-spin current conversion by Dirac surface states of topological insulators, Nat. Phys. **12**, 1027 (2016).

[17] S. Zhang and A. Fert, Conversion between spin and charge currents with topological insulators, Phys. Rev. B **94**, 184423 (2016).

[18] R. Dey, N. Prasad, L. F. Register, and S. K. Banerjee, Conversion of spin current into charge current in a topological insulator: Role of the interface, Phys. Rev. B **97**, 174406 (2016).

[19] J. B. S. Mendes, O. Alves Santos, J. Holanda, R. P. Loreto, C. I. L. de Araujo, C.-Z. Chang, J. S. Moodera, A. Azevedo, and S. M. Rezende, Dirac-surface-state-dominated spin to charge current conversion in the topological insulator $(Bi_{0.22}Sb_{0.78})_2Te_3$ films at room temperature, Phys. Rev. B **96**, 180415(R) (2017).

[20] A. Azevedo, L. H. Vilela-Leão, R. L. Rodríguez-Suárez, A. B. Oliveira, and S. M. Rezende, dc effect in ferromagnetic resonance: Evidence of the spin-pumping effect? J. Appl. Phys. **97**, 10C715 (2005).

[21] S. O. Valenzuela and M. Tinkham, Direct electronic measurement of the spin Hall effect, Nature (London) **442**, 176 (2006).

[22] E. Saitoh, M. Ueda, H. Miyajima, and G. Tatara, Conversion of spin current into charge current at room temperature: Inverse spin-Hall effect, Appl. Phys. Lett. **88**, 182509 (2006).

[23] O. Mosendz, J. E. Pearson, F. Y. Fradin, G. E. W. Bauer, S. D. Bader, and A. Hoffmann, Quantifying Spin Hall Angles from Spin Pumping: Experiments and Theory, Phys. Rev. Lett. **104**, 046601 (2010).

[24] A. Azevedo, L. H. Vilela-Leão, R. L. Rodríguez-Suárez, A. F. Lacerda Santos, and S. M. Rezende, Spin pumping and anisotropic magnetoresistance voltages in magnetic bilayers: Theory and experiment, Phys. Rev. B **83**, 144402 (2011).

[25] L. Liu, C.-F. Pai, Y. Li, H. W. Tseng, D. C. Ralph, and R. A. Buhrman, Spin-torque switching with the giant spin Hall effect of tantalum, Science **336**, 555 (2012).

[26] Y. Kato, R. Myers, A. Gossard, and D. Awschalom, Observation of the spin Hall effect in semiconductors, Science **306**, 1910 (2004).

[27] K. Ando, S. Takahashi, J. Ieda, H. Kurebayashi, T. Trypiniotis, C. H. W. Barnes, S. Maekawa, and E. Saitoh, Electrically tunable spin injector free from the impedance mismatch problem, Nat. Mater. **10**, 655 (2011).

[28] K. Ando and E. Saitoh, Observation of the inverse spin Hall effect in silicon, Nat. Commun. **3**, 629 (2012).

[29] E. Shikoh, K. Ando, K. Kubo, E. Saitoh, T. Shinjo, and M. Shiraishi, Spin-Pump-Induced Spin Transport in p-Type Si at Room Temperature, Phys. Rev. Lett. **110**, 127201 (2013).

[30] J. C. Rojas-Sanchez, M. Cubukcu, A. Jain, C. Vergnaud, Portemont, C. Ducruet, A. Barski, A. Marty, L. Vila J. P. Attane, E. Augendre, G. Desfonds, S. Gambarelli, H. Jaffres, J. M. George, and M. Jamet, Spin pumping and inverse spin Hall effect in germanium, Phys. Rev. B **88**, 064403 (2013).

[31] T. Jungwirth, J. Wunderlich, V. Novák, K. Olejník, B. L. Gallagher, R. P. Campion, K. W. Edmonds, A. W. Rushforth, A. J. Ferguson, and P. Němec, Spin-dependent phenomena and device concepts explored in (Ga,Mn)As, Rev. Mod. Phys. **86**, 855 (2014).

[32] J. B. S. Mendes, S. L. A. Mello, O. Alves Santos, R. O. Cunha, R. L. Rodríguez-Suárez, A. Azevedo, and S. M. Rezende, Inverse spin Hall effect in the semiconductor (Ga,Mn)As at room temperature, Phys. Rev. B **95**, 214405 (2017).

[33] A. Azevedo, O. Alves Santos, G. A. Fonseca Guerra, R. O. Cunha, R. Rodríguez-Suárez, and S. M. Rezende, Competing spin pumping effects in magnetic hybrid structures, Appl. Phys. Lett. **104**, 052402 (2014).

[34] S. S. P. Parkin, K. P. Roche, M. G. Samant, P. M. Rice, and R. B. Beyers, Exchange-biased magnetic tunnel junctions and application to nonvolatile magnetic random access memory, J. Appl. Phys. **85**, 5828 (1999).

[35] J. Nogués and I. K. Schuller, Exchange bias, J. Magn. Magn. Mater. **192**, 203 (1999).

[36] J. R. Fermin, M. A. Lucena, A. Azevedo, F. M. de Aguiar, and S. M. Rezende, Measurements of exchange anisotropy in NiFe/NiO films with different techniques, J. Appl. Phys. **87**, 6421 (2000).

[37] H. Chen, Q. Niu, and A. H. MacDonald, Anomalous Hall Effect Arising from Non Collinear Antiferromagnetism, Phys. Rev. Lett. **112**, 017205 (2014).

[38] J. B. S. Mendes, R. O. Cunha, O. Alves Santos, P. R. T. Ribeiro, F. L. A. Machado, R. L. Rodríguez-Suárez, A. Azevedo, and S. M. Rezende, Large inverse spin Hall effect in the antiferromagnetic metal $Ir_{20}Mn_{80}$, Phys. Rev. B **89**, 140406(R) (2014).

[39] W. Zhang, M. B. Jungfleisch, W. Jiang, J. E. Pearson, and A. Hoffmann, Spin Hall Effects in Metallic Antiferromagnets, Phys. Rev. Lett. **113**, 196602 (2014).

[40] Y. Ou, S. Shi, D. C. Ralph, and R. A. Buhrman, Strong spin Hall effect in the antiferromagnet PtMn, Phys. Rev. B **93**, 220405(R) (2016).

[41] A. H. MacDonald and M. Tsoi, Antiferromagnetic metal spintronics, Philos. Trans. R. Soc. A **369**, 3098 (2011).

[42] E. Gomonay and V. Loktev, Spintronics of antiferromagnetic systems, Low Temp. Phys. **40**, 17 (2014).

[43] T. Jungwirth, X. Marti, P. Wadley, and J. Wunderlich, Antiferromagnetic spintronics, Nat. Nano **11**, 231 (2016).

[44] O. Gomonay, T. Jungwirth, and J. Sinova, Concepts of antiferromagnetic spintronics, Phys. Status Solidi RRL **11**, 1700022 (2017).

[45] M. B. Jungfleisch, W. Zhang, and A. Hoffmann, Perspectives of antiferromagnetic spintronics, Phys. Lett. A **382**, 865 (2018).

[46] V. Baltz, A. Manchon, M. Tsoi, T. Moriyama, T. Ono, and Y. Tserkovnyak, Antiferromagnetic spintronics, Rev. Mod. Phys. **90**, 015005 (2018).

[47] T. Jungwirth, J. Sinova, A. Manchon, X. Marti, J. Wunderlich and C. Felser, The multiple directions of antiferromagnetic spintronics, Nat. Phys. **14**, 200 (2018).

[48] S. Khmelevskyi and P. Mohn, Layered antiferromagnetism with high Neel temperature in the intermetallic compound Mn_2Au, Appl. Phys. Lett. **93**, 162503 (2008).

[49] A. B. Shick, S. Khmelevskyi, O. N. Mryasov, J. Wunderlich, and T. Jungwirth, Spin-orbit coupling induced anisotropy effects in bimetallic antiferromagnets: A route towards antiferromagnetic spintronics, Phys. Rev. B **81**, 212409 (2010).

[50] V. M. T. S. Barthem, C. V. Colin, H. Mayaffre, M. H. Julien and D. Givord, Revealing the properties of Mn_2Au for antiferromagnetic spintronics, Nat. Commun. **4**, 2892 (2013).

[51] M. Jourdan, H. Bräuning, A. Sapozhnik, H.-J.Elmers, H. Zabel, and M. Kläui, Epitaxial Mn_2Au thin films for antiferromagnetic spintronics, J. Phys. D **48**, 385001 (2015).

[52] V. M. T. S. Barthem, C. V. Colin, R. Haettel, D. Dufeu and D. Givord, Easy moment direction and antiferromagnetic domain wall motion in Mn_2Au, J. Magn. Magn. Mater. **406**, 289 (2016).

[53] M. Meinert, D. Graulich, and T. Matalla-Wagner, Electrical Switching of Antiferromagnetic Mn_2Au and the Role of Thermal Activation, Phys. Rev. Appl. **9**, 064040 (2018).

[54] S. Yu. Bodnar, L. Šmejkal, I. Turek, T. Jungwirth, O. Gomonay, J. Sinova, A. A. Sapozhnik, H.-J. Elmers, M. Kläui, and M. Jourdan, Writing and reading Antiferromagnetic Mn_2Au by Néel spin-orbit torques and large anisotropic magnetoresistance, Nat. Commun. **9**, 348 (2018).

[55] M. Arana, F. Estrada, D. S. Maior, J. B. S. Mendes, L. E. Fernandez-Outon, W. A. A. Macedo, V. M. T. S. Barthem, D. Givord, A. Azevedo, and S. M. Rezende, Observation of magnons in Mn_2Au films by inelastic Brillouin and Raman light Scattering, Appl. Phys. Lett. **111**, 192409 (2017).

[56] N. Bhattacharjee, A. A. Sapozhnik, S. Yu. Bodnar, V. Yu. Grigorev, S. Y. Agustsson, J. Cao, D. Dominko, M. Obergfell, O. Gomonay, J. Sinova, M. Kläui, H.-J. Elmers, M. Jourdan, and J. Demsar, Néel Spin-Orbit Torque Driven Antiferromagnetic Resonance in Mn_2Au Probed by Time-Domain THz Spectroscopy, Phys. Rev. Lett. **120**, 237201 (2018).

[57] S. M. Rezende and F. M. de Aguiar, Spin wave instabilities, auto-oscillations and chaos in yttrium-iron-garnet, Proc. IEEE **78**, 893 (1990).

[58] R. W. Damon and J. R. Eshbach, Magnetostatic modes of a ferromagnetic slab, J. Appl. Phys. **31**, S104 (1960).

[59] C. Kittel, Interpretation of anomalous larmor frequencies in ferromagnetic resonance experiment, Phys. Rev. **71**, 270 (1947).

[60] Y. Tserkovnyak, A. Brataas, and G. E. Bauer, Enhanced Gilbert Damping in Thin Ferromagnetic Films, Phys. Rev. Lett. **88**, 117601 (2002).

[61] Y. Tserkovnyak, A. Brataas, G. E. W. Bauer, and B. I. Halperin, Nonlocal magnetization dynamics in ferromagnetic heterostructures, Rev. Mod. Phys. **77**, 1375 (2005).

[62] Silsbee *et al.*, Coupling between ferromagnetic and conduction-spin-resonance modes at a ferromagnetic–normal-metal interface, Phys. Rev. B **19**, 4382 (1979)

[63] A. Azevedo, R. O. Cunha, F. Estrada, O. Alves Santos, J. B. S. Mendes, L. H. Vilela-Leão, R. L. Rodríguez-Suárez, and S. M. Rezende, Electrical detection of ferromagnetic resonance in single layers of permalloy: Evidence of magnonic charge pumping, Phys. Rev. B **92**, 024402 (2015).

[64] C. W. Sandweg, Y. Kajiwara, K. Ando, E. Saitoh, and B. Hillebrands, Enhancement of the spin pumping efficiency by spin wave mode selection, Appl. Phys. Lett. **97**, 252504 (2010).

[65] L. H. Vilela-Leão, C. Salvador, A. Azevedo, and S. M. Rezende, Unidirectional anisotropy in the spin pumping voltage in yttrium iron garnet/platinum bilayers, Appl. Phys. Lett. **99**, 102505 (2011).

[66] S. M. Rezende, R. L. Rodríguez-Suárez, and A. Azevedo, Magnetic relaxation due to spin pumping in thick ferromagnetic films in contact with normal metals, Phys. Rev. B **88**, 014404 (2013).

[67] M. Weiler, M. Althammer, M. Schreier, J. Lotze, M. Pernpeintner, S. Meyer, H. Huebl, R. Gross, A. Kamra, J. Xiao, Y. T. Chen, H. J. Jiao, G. E. W. Bauer, S. T. B. Goennenwein, M. Weiler *et al.*, Experimental Test of the Spin Mixing Interface Conductivity Concept, Phys. Rev. Lett. **111**, 176601 (2013).

[68] C. Hahn, G. de Loubens, M. Viret, and O. Klein, Detection of Microwave Spin Pumping Using the Inverse Spin Hall Effect, Phys. Rev. Lett. **111**, 217204 (2013).

[69] C. Du, H. Wang, P. Chris Hammel, and F. Yang, $Y_3Fe_5O_{12}$ spin pumping for quantitative understanding of pure spin transport and spin Hall effect in a broad range of materials, J. Appl. Phys. **117**, 172603 (2015).

[70] M. B. Jungfleisch, A. V. Chumak, A. Kehlberger, V. Lauer, D. H. Kim, M. C. Onbasli, C. A. Ross, M. Kläui, and B. Hillebrands, Thickness and power dependence of the spin-pumping effect in $Y_3Fe_5O_{12}$/Pt heterostructures measured by the inverse spin Hall effect, Phys. Rev. B **91**, 134407 (2015).

[71] D. M. Pozar, *Microwave Engineering* (Wiley, New York, 2012).

[72] Y. Wang, P. Deorani, X. Qiu, J. H. Kwon, and H. Yang, Determination of intrinsic spin Hall angle in Pt, Appl. Phys. Lett. **105**, 152412 (2014)

[73] K. Uchida, H. Adachi, T. Ota, H. Nakayama, S. Maekawa, and E. Saitoh, Observation of longitudinal spin-Seebeck effect in magnetic insulators, Appl. Phys. Lett. **97**, 172505 (2010).

[74] G. E. W. Bauer, E. Saitoh, and B. J. van Wees, Spin caloritronics, Nat. Mater. **11**, 391 (2012).

[75] T. Kikkawa, K. Uchida, Y. Shiomi, Z. Qiu, D. Hou, D. Tian, H. Nakayama, X.-F. Jin, and E. Saitoh, Longitudinal Spin Seebeck Effect Free from the Proximity Nernst Effect, Phys. Rev. Lett. **110**, 067207 (2013).

[76] S. M. Rezende, R. L. Rodríguez-Suárez, R. O. Cunha, A. R. Rodrigues, F. L. A. Machado, G. A. Fonseca Guerra, J. C. Lopez Ortiz, and A. Azevedo, Magnon spin-current theory for the longitudinal spin-Seebeck effect, Phys. Rev. B **89**, 014416 (2014).

[77] S. R. Boona, R. C. Myers, and J. P. Heremans, Spin caloritronics, Energy Environ. Sci. **7**, 885 (2014).

[78] K. Uchida, M. Ishida, T. Kikkawa, A. Kirihara, T. Murakami, and E. Saitoh, Longitudinal spin Seebeck effect: from fundamentals to applications, J. Phys.: Condens. Matter **26**, 343202 (2014).

[79] K. Uchida, H. Adachi, T. Kikkawa, A. Kirihara, M. Ishida, S. Yorozu, S. Maekawa, and E. Saitoh, Thermoelectric generation based on spin Seebeck effects, Proc. IEEE **104**, 1946 (2016).

[80] S. M. Rezende, R. L. Rodríguez-Suárez, J. C. López Ortiz, and A. Azevedo, Bulk magnon spin current theory for the longitudinal spin Seebeck effect, J. Magn. Magn. Mater. **400**, 171 (2016).

[81] H. Yu, S. D. Brechet, and J.-P. Ansermet, Spin caloritronics, origin and outlook, Phys. Lett. A **381**, 825 (2017).

[82] S. M. Rezende, A. Azevedo, and R. L. Rodríguez-Suárez, Magnon diffusion theory for the spin Seebeck effect in ferromagnetic and antiferromagnetic insulators, J. Phys. D **51**, 174004 (2018).